

UV to radio centimetric spectral energy distributions of optically-selected late-type galaxies in the Virgo cluster^{★,★★}

A. Boselli¹, G. Gavazzi², and G. Sanvito²

¹ Laboratoire d'Astrophysique de Marseille, BP 8, Traverse du Siphon, 13376 Marseille Cedex 12, France

² Università degli Studi di Milano-Bicocca, Dipartimento di Fisica, Piazza dell'Ateneo Nuovo 1, 20126 Milano, Italy
e-mail: Giuseppe.Gavazzi@mib.infn.it; Gerry.Sanvito@mib.infn.it

Received 10 October 2002 / Accepted 16 December 2002

Abstract. We present a multifrequency dataset for an optically-selected, volume-limited, complete sample of 118 late-type galaxies ($\geq S0a$) in the Virgo cluster. The database includes UV, visible, near-IR, mid-IR, far-IR, radio continuum photometric data as well as spectroscopic data of H α , CO and HI lines, homogeneously reduced, obtained from our own observations or compiled from the literature.

Assuming the energy balance between the absorbed stellar light and that radiated in the IR by dust, we calibrate an empirical attenuation law suitable for correcting photometric and spectroscopic data of normal galaxies. The data, corrected for internal extinction, are used to construct the spectral energy distribution (SED) of each individual galaxy, and combined to trace the median SED of galaxies in various classes of morphological type and luminosity. Low-luminosity, dwarf galaxies have on average bluer stellar continua and higher far-IR luminosities per unit galaxy mass than giant, early-type spirals. If compared to nearby starburst galaxies such as M 82 and Arp 220, normal spirals have relatively similar observed stellar spectra but 10–100 times lower IR luminosities. The temperature of the cold dust component increases with the far-IR luminosity, from giant spirals to dwarf irregulars. The SED are used to separate the stellar emission from the dust emission in the mid-IR regime. We show that the contribution of the stellar emission at 6.75 μm to the total emission of galaxies is generally important, from $\sim 80\%$ in Sa to $\sim 20\%$ in Sc.

Key words. galaxies: general – galaxies: spiral – galaxies: ISM – galaxies: stellar content

1. Introduction

An ideal tool for constraining observationally models of galaxy evolution would consist of a multi-dimensional “data-cube”: $D_{\text{imag}}(\lambda, \text{Type}, \text{Lum}, z, \text{Env})$ containing imaging data of complete samples of galaxies, spanning the broadest possible wavelength (λ), redshift (z), morphological type (*Type*) and luminosity (*Lum*) ranges. Moreover, all environmental conditions (*Env*) should be equally represented, from the coarsest “field” to the densest cluster’s cores.

Such an ideal data-base is unrealistic. First of all, multifrequency images hardly exist, at suitable resolution, even for galaxies in the Local Group. The requirement that the data-cube consists of “imaging” data must then be relaxed for the more realistic requirement that it should contain “integrated”

data, as more commonly available from aperture/CCD photometry. Even with these reduced characteristics, very few such data-sets exist either for high z , or for local galaxies. The presently available samples cover a small wavelength window, such as those of Connolly et al. (1995) or Kinney et al. (1993), or they are biased towards starburst and active galaxies (Schmitt et al. 1997), thus they are not representative of “normal” galaxies.

Within few years from now, however, when SLOAN will reach completion and the space missions GALEX (UV) and ASTRO-F (FIR) will perform their all-sky surveys, large data-sets meeting the above requirements will be at hands.

There is yet a sample which approaches the ideal requirements. The data-cube we are referring to is an optically selected (complete) one, representative of galaxy in a broad luminosity range and it is truly multifrequency (from the far-UV to the radio domains). It suffers from three limitations: it is local ($z = 0$) and it represents only late-type galaxies in the densest environment, being composed of galaxies in the the Virgo cluster: $D_{\text{phot}}(\text{UV} - \text{radio}, \text{Late}, \text{Lum}, z = 0, \text{Virgo})$. It is on this data-base that the present paper is focused.

Send offprint requests to: A. Boselli,
e-mail: Alessandro.Boselli@oamp.fr

* Tables 2–5, 7, 8, and Fig. 2 are only available in electronic form at <http://www.edpsciences.org>

** Tables 10–12 are only available in electronic form at the CDS via anonymous ftp to cdsarc.u-strasbg.fr (130.79.128.5) or via <http://cdsweb.u-strasbg.fr/cgi-bin/qcat?J/A+A/402/37>

Skipping through the details of the sample selection and of the available data that can be found in Sects. 2 and 3 of this paper respectively, it is worth spending some words on what scientific purposes such data-base is aimed at.

Individual galaxies are represented in the data-base under the form of Spectral Energy Distributions (SEDs), such as those presented in Fig. 2. SEDs are powerful diagnostic tools for studying the energy balance between the principal constituents of galaxies. From 0.1 to 5 μm (UV, Visible, Near-IR) SEDs are dominated by the stellar thermal radiation, (but include most of the measurable recombination lines providing the diagnostics of the ISM). From 5 to 25 μm (Mid-IR) the dominant source is the radiation from very small grains of dust, but the contribution of emission lines (PAH) is relevant. From 25 to 1000 μm (Far-IR, sub-mm radio) the flux of SEDs is due to the thermal radiation from cold dust (10–100 K). Important diagnostic lines such as the [CII] ($\lambda 158 \mu\text{m}$) and CO are found in this interval. It is here that dust-rich objects peak their flux distributions. At wavelengths longer than 1 cm (radio) the radiation is non-thermal (synchrotron) by relativistic cosmic ray electrons and magnetic fields, but the most important ISM diagnostic line, the 21 cm line of the neutral hydrogen, lies in this domain. All these components and their complex feedback relations can be studied at once using the SEDs. First an estimate of the relative fraction of stars in the various age (temperature) classes can be obtained by fitting populations synthesis models (Bruzual & Charlot 1993) to the stellar continua (see e.g., Gavazzi et al. 2002a). Once the stellar populations are determined, by studying the ISM emission line properties (e.g. the H α) one can learn about the ionization processes in HII regions. From the FIR properties we can study the dust heating mechanisms. Finally from the luminosity of the synchrotron radiation one can study the contribution of the various stellar populations to the cosmic ray acceleration.

Before energy balances can be quantitatively derived, however, the observed SEDs must be properly corrected for a number of effects that introduce wavelength dependent distortions to their shape. Primarily the SEDs must be rest-framed. Galaxies at large redshift require important K corrections. Their cosmic evolution can be studied by comparing their rest-frame SEDs with those of normal local galaxies. Hence the importance of obtaining template SEDs representative of normal galaxies, unlike those of starburst galaxies such as M 82 or Arp 220 (see Fig. 3), often used for such a purpose.

Secondly comes the internal extinction correction. Stellar light is absorbed and scattered by the dust in a wavelength dependent way. Corrected SEDs can be derived if the proper amount of extinction is estimated. The amount of stellar light absorbed in the blue should equal that thermally re-emitted in the FIR by the dust. Thus the difference of the integral under the stellar continua in the SEDs before and after the extinction correction gives the energy radiated in the FIR. By reversing the argument Buat et al. (2002) derive a robust estimate of the internal extinction in normal galaxies.

Finally the comparison of SEDs of isolated and cluster galaxies can shed light on influences of the environment on the various components of galaxies. Our Virgo sample, spanning

a large interval of galactocentric projected distance from M 87 (up to 6 degrees), provides a clue also on this issue.

Matter in the present paper is organized as follows The sample is described in Sect. 2; in Sect. 3 we give a new prescription for the determination of the UV, optical and near-IR internal extinction based on the FIR/UV flux ratio. The adopted extinction law is checked in Sect. 5.3 using considerations on the energy balance between the emitted far-IR radiation and the absorbed stellar light. The SEDs of the sample galaxies are presented in Sect. 4, and analyzed in Sect. 5. We construct template SEDs in bins of equal morphological type and luminosity and compare them to those of starburst galaxies (Sect. 5.1). The stellar contribution to the mid-IR emission of galaxies (Sect. 5.2) and the properties of the nonthermal radiation (Sect. 5.4) are also analyzed. The bolometric properties of the observed sample are described in Sect. 5.5.

New optical observations obtained using the 1.2 m telescope of the Observatoire de Haute Provence (OHP), the 0.9 m telescope at Kitt Peak and the 2.5 m INT telescope at el Roques de los Muchachos (La Palma) are given in the appendix.

All observations analyzed in the present paper are contained in a database that has been made available to the international community via the Word Wide Web site GOLDMine (<http://goldmine.mib.infn.it>) described in Gavazzi et al. (2003).

2. The sample

The sample analyzed in this work was extracted from the optically selected Virgo Cluster Catalogue (VCC) of Binggeli et al. (1985), which is complete to $B_T \leq 18$. Galaxies were selected according to the following criteria:

- $B_T < 18$;
- Hubble type later than S0;
- classified as cluster member by Binggeli et al. (1985, 1993);
- lying at a projected angular distance smaller than 2 degrees from M 87 (cluster-core) or greater than 4 degrees from the position of maximum projected galaxy density given by Sandage et al. (1985) (cluster-periphery), but excluding galaxies within 1.5 degrees of the M 49 sub-cluster;
- to limit the spread of distances within the sample, galaxies in the M and W clouds, and in the Southern Extension ($\delta(1950) < 5^\circ$) were also excluded¹.

The sky areas from which galaxies were chosen define two contrasting subsamples to optimise the statistical evaluation of the cluster environment on observed properties (see Fig. 1). The cluster-core subsample is composed of 46 galaxies within the X-ray emitting “atmosphere” of M 87. The cluster-periphery subsample includes 72 galaxies in the outskirts.

The resulting sample of 118 galaxies is complete to $B_T = 18$, and both the cluster-periphery and -core subsamples

¹ Some galaxies belonging to these three substructures are lying outside the regions delimited as M and W clouds and Southern Extension in Fig. 1.

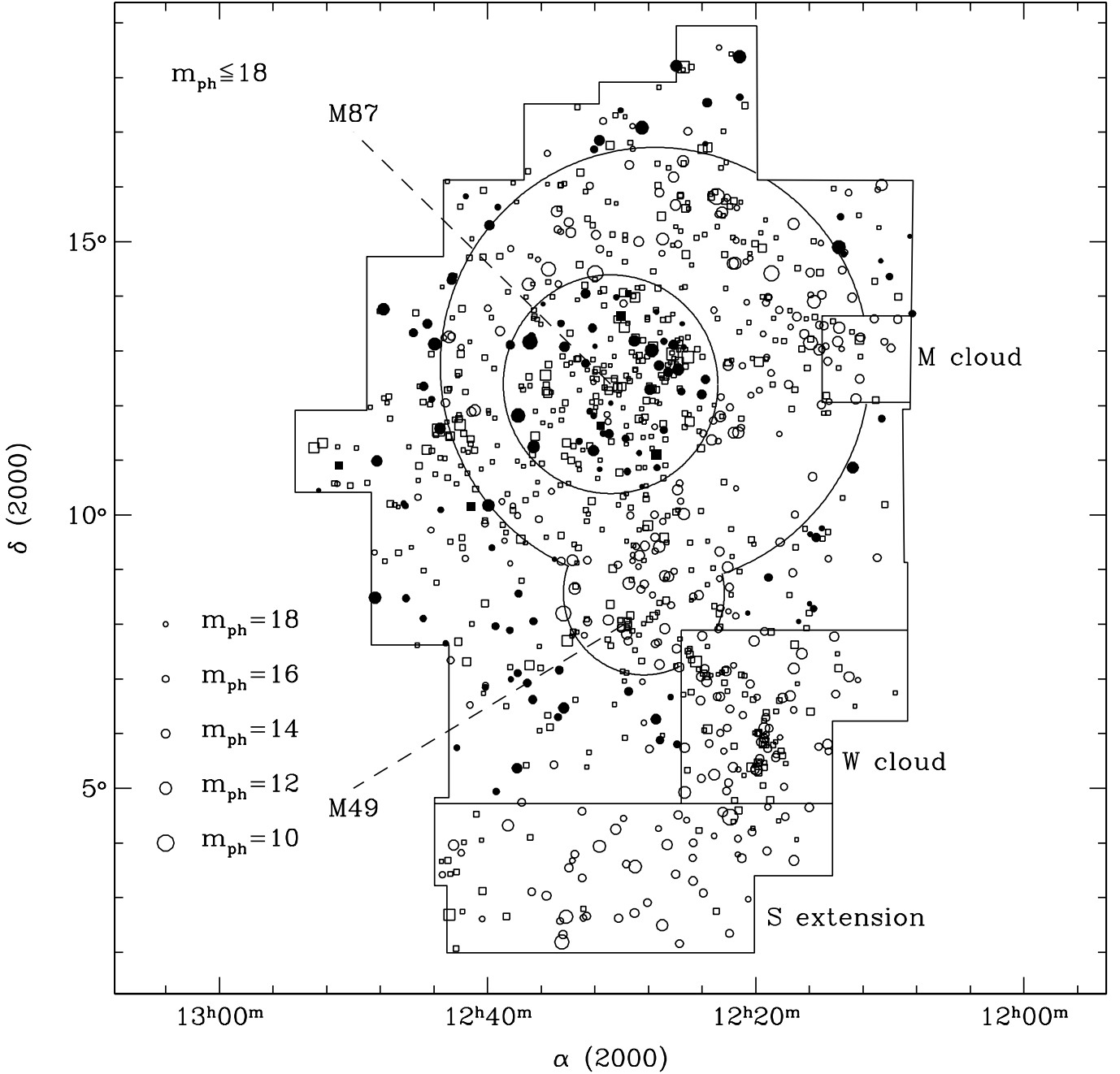


Fig. 1. Plot of all VCC galaxies classified as members by Binggeli et al. (1985) taken from Fig. 1 of Sandage et al. (1985). The subsample of galaxies here analyzed (see Sect. 2) are marked with filled symbols of increasing size according to their magnitude. Empty symbols are for Virgo members not included in the ISO sample; circles for late-type galaxies (\geq Sa), squares for early types (\leq S0a). The 2.0 degree radius circle centred on M 87 contains the cluster-core subsample. The inner boundary of the cluster periphery subsample has a radius of 4 degrees about the position of maximum projected galaxy density. The 1.5 degree radius circle is centered on the position of maximum projected galaxy density of M 49 subcluster.

span the range $-21 < M_B < -13$. Both subsamples are approximately equally divided between giant spirals on the one hand and dwarf and irregular galaxies on the other. The distribution over Hubble type is summarised in Table 1.

The parameter of the sample galaxies are given in Table 2, arranged as follows:

- Column 1: VCC denomination (Binggeli et al. 1985).
- Column 2: NGC name.
- Column 3: IC name.
- Column 4: UGC name (Nilson 1973).
- Column 5: CGCG denomination (Zwicky et al. 1961–68)
- Columns 6 and 7: (B2000.0) celestial coordinates, from NED, with a few arcsec accuracy.
- Column 8: morphological type, from the VCC or from Binggeli et al. (1993).
- Column 9: photographic magnitude from the VCC.

Table 1. Distribution of sample over Hubble type for the cluster-periphery and cluster-core subsamples.

	S0/a – Sab	Sb – Sc	Scd – Sm	Im	BCD
periphery	9	16	12	20	15
core	16	11	6	10	3
Total	25	27	18	30	18

- Columns 10 and 11: major (a) and minor (b) optical diameters (arcmin) determined at the surface brightness of 25th mag arcsec⁻². For galaxies without a 25th mag arcsec⁻² value in the VCC, the diameter is computed from the “last visible” isophotal diameter given in the VCC using the relation: $\text{Log } a_{\text{ext}}(b_{\text{ext}}) = 0.99\text{Log } a(b) + 0.1$.
- Column 12: heliocentric velocity, in km s⁻¹.
- Column 13: distance, in Mpc. Distances to the various substructures of Virgo are as given in Gavazzi et al. (1999).
- Column 14: cluster membership as defined in Gavazzi et al. (1999)².
- Column 15: projected angular separation from the cluster centre (M87), in degrees.
- Column 16: the model-independent near-IR concentration index parameter C_{31} , from Gavazzi et al. (2000), defined as the ratio between the radii that enclose 75% and 25% of the total light. C_{31} is a tracer of the light distribution within galaxies: values of $C_{31} < 3$ are for pure exponential discs, $C_{31} > 3$ for galaxies with bulges.
- Column 17: notes.

3. The data

The SED presented in this paper have been constructed using multifrequency data available in the literature or from our own observations, treated as consistently as possible, in order to produce an homogeneous data-set.

The UV data are taken from the FAUST (Lampton et al. 1990) and the FOCA (Milliard et al. 1991) experiments. In order to be consistent with our previous works, we transformed UV magnitudes taken at 1650 Å by Deharveng et al. (1994) to 2000 Å assuming a constant colour index $\text{UV}(2000) = \text{UV}(1650) + 0.2$ mag. This relation has been obtained by comparing the FAUST 1650 Å with the SCAP (Donas et al. 1987) 2000 Å UV magnitudes of 17 late-type galaxies in the Virgo cluster, observed by both experiments (Deharveng et al. 1994). FOCA magnitudes are from Deharveng et al. (2002), and Donas et al., in preparation. These are total magnitudes, determined by integrating the UV emission up to the weakest detectable isophote. The estimated error on the UV magnitude is 0.3 mag in general, but it ranges from 0.2 mag for bright galaxies to 0.5 mag for weak sources observed in frames with larger than average calibration uncertainties.

² The Gavazzi et al. (1999) cluster membership criterion, based on the 3D distribution of galaxies in the Virgo cluster, is slightly different from that given by Binggeli et al. (1985, 1993), used to define the sample. It is thus not surprising that several objects in Table 2 are listed as members of cluster B or of the M and W clouds.

U , B and V photometry is generally derived from our own CCD measurements consistently with Gavazzi & Boselli (1996), as described in the appendix. When these are not available it is derived from aperture photometry taken from the literature. The (U, B, V) D_{25} magnitudes, computed at the 25th mag arcsec⁻² isophotal B band diameter as in Gavazzi & Boselli (1996), have ~10% uncertainty. They are on average 0.1 mag fainter than the total asymptotic magnitudes.

NIR data, from Nicmos3 observations, are taken mostly from Boselli et al. (1997) and Gavazzi et al. (2001). Magnitudes (J, H, K) are determined consistently with the optical magnitudes as in Gavazzi & Boselli (1996). The typical uncertainty in (J, H, K) is 10%. As for the visible magnitudes, they are on average 0.1 mag fainter than the total asymptotic magnitudes.

Mid-IR data, at 6.75 and 15 μm , are from Boselli et al. (2003). Flux densities have been extracted from ISOCAM images by integrating the emission until the weakest detectable isophote. Even if the mid-IR emission of these galaxies is less extended than in the visible and near-IR bands, ISOCAM data provide us with integrated flux densities representative of the whole galaxy. The typical uncertainty on the ISOCAM data is ~30%.

12, 25, 60 and 100 μm integrated flux densities from the IRAS survey are taken from different sources. The typical uncertainty in the IRAS data is ~15%. Alternative Far-IR values at 60 and 100 μm from ISOPHOT, as well as 170 μm flux densities, are taken from Tuffs et al. (2002), with a typical nominal uncertainty of ~10%. The comparison of ISO and IRAS data for the sample galaxies detected in both surveys reveals a systematic difference of $\text{ISO/IRAS} = 0.95$ and 0.82 at 60 and 100 μm respectively (Tuffs et al. 2002).

We collected radio continuum data at 2.8, 6.3, 12.6 and 21 cm from different sources. 21 cm radio continuum data, available for the whole sample, are mostly from the NVSS survey (Condon et al. 1998) (see Gavazzi & Boselli 1999). All radio continuum data are integrated fluxes. The typical uncertainty is ~20%.

The photometric data for the whole sample are given in Table 3, arranged as follows:

- Column 1: VCC denomination.
- Column 2: UV magnitude at 2000 Å, uncorrected for galactic and internal extinction.
- Columns 3–8: U, B, V, J, H, K magnitudes in the Johnson system, determined as described in Gavazzi & Boselli (1996), uncorrected for galactic and internal extinction.
- Column 9: ISOCAM 6.75 μm flux density, in mJy.
- Column 10: IRAS 12 μm flux density, in mJy.
- Column 11: ISOCAM 15 μm flux density, in mJy.
- Column 12: IRAS 25 μm flux density, in mJy.
- Column 13: IRAS 60 μm flux density, in mJy.
- Column 14: ISOPHOT 60 μm flux density, in mJy.
- Column 15: IRAS 100 μm flux density, in mJy.
- Column 16: ISOPHOT 100 μm flux density, in mJy.
- Column 17: ISOPHOT 170 μm flux density, in mJy.
- Columns 18–21: radio continuum flux densities at 2.8, 6.3, 12.6 and 21 cm, in mJy.

All data given in Table 3 are observed quantities. The UV, optical and near-IR data are uncorrected for dust extinction, the mid-IR data for the contribution of the stellar component, the radio continuum data for the contribution of the nuclear emission.

References to the photometric data are given in Table 4.

Additional emission line data are given in Table 5, arranged as follows:

- Column 1: VCC denomination.
- Column 2: $H\alpha$ + $[NII]$ equivalent width, in \AA .
- Column 3: logarithm of the $H\alpha$ + $[NII]$ line, in $\text{erg cm}^{-2} \text{s}^{-1}$.
- Column 4: reference to the $H\alpha$ data.
- Column 5: logarithm of the HI mass, in solar units, defined as $MHI = 2.36 \cdot 10^5 D^2 S HI$, where D is the distance of the galaxy in Mpc (from Table 2), and $S HI$ is the integrated HI flux, in Jy km s^{-1} .
- Column 6: the HI-deficiency parameter, defined as the ratio of the HI mass to the average HI mass of isolated objects of similar morphological type and linear size (Haynes & Giovanelli 1984); it is used to discriminate between “normal” galaxies and galaxies suffering for gas depletion due to ram pressure. Galaxies with an HI-deficiency parameter ≤ 0.3 can be treated as unperturbed, isolated galaxies.
- Column 7: the quality of the HI profile: 1 stands for high signal to noise, two-horns profiles, 2 for high signal to noise Gaussian profiles, 3 for average signal to noise profiles, 4 for poor quality data and 5 for those objects whose profile is not available in the literature.
- Column 8: HI line width, measured as the average value of the width at 20 and 50% of the peak, in km s^{-1} .
- Column 9: reference to the HI data.
- Column 10: logarithm of the H_2 mass, in solar units, defined as in Boselli et al. (2002b), determined assuming a luminosity dependent X conversion factor between the CO intensity and the H_2 surface density $\log X = -0.38 \log L_H + 24.23 \text{ mol cm}^{-2} (\text{K km s}^{-1})^{-1}$. As shown in Boselli et al. (2002b), the use of a luminosity dependent rather than a metallicity dependent X conversion factor does not affect the uncertainty in the determination of the molecular hydrogen mass.
- Column 11: reference to the CO data.

3.1. The extinction correction

UV to near-IR data have been corrected for galactic extinction according to Burstein & Heiles (1982). The galactic extinction $A_g(B)$, taken from NED and listed in Table 7, have been transformed to $A_g(\lambda)$ assuming a standard galactic extinction law (see Table 6): $A_g(\lambda) = c(\lambda) A_g(B)$, where $c(\lambda) = k(\lambda)/k(B)$.

The observed stellar radiation of galaxies, from UV to near-IR wavelengths, is subject to internal extinction (absorption plus scattering) by the interstellar dust. In order to quantify the emission of the various stellar populations, UV, optical and, to a lesser amount, near-IR fluxes must be corrected for dust attenuation. Furthermore, since dust extinction varies from galaxy to galaxy (according to their geometrical parameters such as the inclination, their history of star formation and metallicity),

Table 6. Galactic extinction law.

Filter	λ	$c(\lambda)$
	\AA	
UV	2000	2.10
<i>U</i>	3650	1.15
<i>B</i>	4400	1.00
<i>V</i>	5500	0.75
<i>J</i>	12 500	0.21
<i>H</i>	16 500	0.14
<i>K'</i>	21 000	0.10

corrections appropriate to each individual galaxy must be determined.

Estimating the dust extinction at different λ in external galaxies is however very difficult (it has been done only for the Magellanic clouds). Buat et al. (2002) have shown that, for example, the Calzetti’s law calibrated on the central part of starburst galaxies (Calzetti 2001) strongly overestimates the extinction in normal, late-type objects. This difficulty is mainly due to two reasons: a) the extinction strongly depends on the relative geometry of the emitting stars and of the absorbing dust within the disc of galaxies. The young stellar population are mostly located along the disc in a thin layer, while the old populations forms a thicker layer. This point is further complicated by the fact that different dust components (very small grains, big grains etc.), which have different opacities to the UV, visible or near-IR light, have themselves different geometrical distributions both on the large and small scales. b) it is still uncertain whether the Galactic extinction law is universal, or if it changes with metallicity and/or with the UV radiation field. Detailed observations of resolved stars in the Small Magellanic Cloud by Bouchet et al. (1985) indicate that the extinction law in the optical domain is not significantly different from the Galactic one in galaxies with a UV field ~ 10 times higher and a metallicity ~ 10 times lower than those of the Milky Way. A steeper UV rise and a weaker 2200 \AA bump than in the Galactic extinction law have been however observed in the LMC and SMC (Mathis 1990).

While the adoption of the Galactic extinction law for external galaxies seems reasonable (even though it is questionable for low-luminosity galaxies), no simple analytic functions describing the geometrical distribution of emitting stars and absorbing dust, both on small and large scales, are yet available.

The radiative transfer models of Witt & Gordon (2000) have however shown that the FIR to UV flux ratio, being mostly independent of the geometry, of the star formation history (the two radiations are produced by similar stellar populations) and of the adopted extinction law, is a robust estimator of the dust extinction at UV wavelengths. Here we will use this method to estimate the extinction correction in the UV, the wavelength most affected by dust.

We propose an internal extinction correction prescription similar to that described in Gavazzi et al. (2002a).

Our semi-empirical determination of $A(\text{UV})$ takes into account the scattered light. Following Buat et al. (1999), we estimate $A_i(\text{UV})$ from the relation:

$$A_i(\text{UV}) = 0.466 + \text{Log}(\text{FIR}/\text{UV}) + 0.433 \times (\text{Log}(\text{FIR}/\text{UV}))^2 \quad [\text{mag}] \quad (1)$$

where

$$\text{FIR} = 1.26 \times (2.58 \times 10^{12} \times F_{60} + 10^{12} \times F_{100}) \times 10^{-26} \quad [\text{Wm}^{-2}] \quad (2)$$

F_{60} and F_{100} are the IRAS FIR fluxes (in Jy) and

$$\text{UV} = 10^{-3} \times 2000 * 10^{(\text{UV}_{\text{mag}}+21.175)/-2.5} \quad [\text{Wm}^{-2}]. \quad (3)$$

$A_i(\lambda)$ can be derived from $A_i(\text{UV})$ once an extinction law and a geometry for the dust and star distribution are assumed. We adopt the sandwich model, where a thin layer of dust of thickness ζ is embedded in a thick layer of stars:

$$A_i(\lambda) = -2.5 \cdot \log \left(\left[\frac{1 - \zeta(\lambda)}{2} \right] \left(1 + e^{-\tau(\lambda) \cdot \sec(i)} \right) + \left[\frac{\zeta(\lambda)}{\tau(\lambda) \cdot \sec(i)} \right] \cdot \left(1 - e^{-\tau(\lambda) \cdot \sec(i)} \right) \right) \quad [\text{mag}] \quad (4)$$

where the dust to stars scale height ratio $\zeta(\lambda)$ depends on λ (in units of \AA) as:

$$\zeta(\lambda) = 1.0867 - 5.501 \times 10^{-5} \cdot \lambda. \quad (5)$$

Relation (5) has been calibrated adopting the average between the optically thin and optically thick cases with λ dependent dust to star scale height ratios given by Boselli & Gavazzi (1994). Observations of some edge-on nearby galaxies show that it is still unclear whether ζ depends or not on λ (Xilouris et al. 1999). As shown in Gavazzi et al. (2002a), however, similar values of $A_i(\lambda)$ are obtained in the case of a sandwich model and of the extreme case of a slab model ($\zeta = 1$), meaning that the high uncertainty on ζ is not reflected on $A_i(\lambda)$.

In the case of the UV band ($\lambda = 2000 \text{\AA}$), $\zeta = 1$, and Eq. (4) reduces to a simple slab model. In this case $\tau(\text{UV})$ can be derived by inverting Eq. (4):

$$\tau(\text{UV}) = [1/\sec(i)] \cdot \left(0.0259 + 1.2002 \times A_i(\text{UV}) + 1.5543 \times A_i(\text{UV})^2 - 0.7409 \times A_i(\text{UV})^3 + 0.2246 \times A_i(\text{UV})^4 \right) \quad (6)$$

using the galactic extinction law $k(\lambda)$ (Savage & Mathis 1979), we then derive:

$$\tau(\lambda) = \tau(\text{UV}) \cdot k(\lambda)/k(\text{UV}) \quad (7)$$

and we compute the complete set of $A_i(\lambda)$ using Eq. (4).

FIR/UV is available for 44 objects. If FIR or UV measurements are unavailable we assume the average values $A_i(\text{UV}) = 1.28; 0.85; 0.68 \text{ mag}$ for Sa-Sbc; Sc-Scd; Sd-Im-BCD galaxies respectively, as determined when FIR and UV measurements are available.

Once corrected adopting the aforementioned prescription, we checked empirically that the SED do not contain a residual dependence on galaxy inclination. The corrected SEDs of 32 Sc galaxies, binned in 4 intervals of inclination, and their fit parameters were found very consistent one another. The galactic and internal extinction correction (in magnitude) for the observed galaxies are given in Table 7.

This empirical attenuation law gives a zeroth order estimate of the attenuation in the UV regime, the most affected by dust. We stress however that the shape of the corrected spectrum, in particular at UV wavelengths, is still uncertain. This is due not only to the lack of observational constraints other than the 2000\AA flux, but also to the large uncertainties on the relative geometrical distributions of dust and stars and on the extinction law, which might significantly depend on the UV field and metallicity in this wavelength regime.

4. The SEDs

Figure 2 shows the SEDs of the sample galaxies obtained using the data given in Table 3 (only for those galaxies with at least 2 photometric data points). UV, optical and near-IR data are corrected for galactic and internal extinction as described in the previous section. FIR data at 60 and $100 \mu\text{m}$ are average values between IRAS and ISOPHOT data when both are available. When one of the two data is an upper limit, we take the detection³. To be as consistent as possible with IRAS, ISOPHOT data have been corrected for the average ISOPHOT/IRAS ratio found by Tuffs et al. (2002) for Virgo galaxies detected with both instruments, ISOPHOT/IRAS = 0.95 and 0.82 at 60 and $100 \mu\text{m}$ respectively.

The morphological type given in Table 2 and the logarithm of the H band luminosity, defined as $\log L_H = 11.36 - 0.4H_T + 2 \log D$ (in solar units), where H_T is the total H band magnitude and D is the distance to the source (in Mpc), are labeled in Fig. 2. For few objects we derive the H luminosity from K band measurements assuming an average $H-K$ colour of 0.25 mag (independent of type; see Gavazzi et al. 2000). A minority of the objects in our sample have an H band magnitude obtained from aperture photometry, thus with no asymptotic extrapolation. For these we use the H magnitude determined as in Gavazzi & Boselli (1996) at the optical radius which is on average 0.1 mag fainter than H_T (Gavazzi et al. 2000).

The continuum line in the optical domain gives the integrated spectrum obtained by Gavazzi et al. (2002a). The two dashed lines at $\lambda < 10 \mu\text{m}$ are the Bruzual & Charlot stellar population synthesis models (GISSEL 2001). The upper curves represent the models which best fit the extinction corrected data, as determined by Gavazzi et al. (2002a). The lower curves represent the same models attenuated by dust extinction using the inverse relations of Sect. 3.1. For galaxies with insufficient photometric points for fitting a model, we adopt the Bruzual & Charlot model that best-fits a template SED of similar morphological type (Fig. 9 in Gavazzi et al. 2002a). To be

³ The IRAS data of VCC 17 and 1725 from Almozno & Brosch (1998) are inconsistent with the PHOT data of Tuffs et al. (2002) and with our CAM data, and are thus not used in the construction of these SEDs.

consistent with Gavazzi et al. (2002a), all models are normalized to the V band photometric data when available, or to the K band. Given the poor quality of the fit, models are not shown for the galaxies VCC 1217 and VCC 1313.

We have preferred not to give fits in the Mid-IR range for two reasons: 1) because the very small grains and the carriers of the Aromatic Infrared Bands responsible for the mid-IR dust emission are not in thermal equilibrium with the radiation, but are stochastically heated (mostly) by UV photons (Boselli et al. 2003). Thus modified black-body functions cannot be used to fit the mid-IR data. 2) mid-IR spectra obtained with the CVF camera onboard ISO in various galactic and extragalactic environments has shown a variety of strong emission lines with fluxes comparable with the continuum. It is thus difficult to estimate a typical mid-IR spectrum of galaxies.

The dashed line in the FIR domain (20–2000 μm) represents a two dust components model. Two modified blackbodies $F(\nu) \sim \nu^\beta B(\nu)(T_D)$, with $\beta = 2$, one with a fixed warm temperature of $T_w = 47$ K (tracing the star forming regions), the other with a (variable) cold temperature T_c (tracing the cirrus emission), were determined consistently with Popescu et al. (2002). The two components are calibrated to match the 60 and 170 μm data respectively. For galaxies not observed by PHOT but detected by IRAS at 60 and 100 μm , we adopted a modified blackbody with $T_w = 47$ K for the warm component and we assume $T_c = 18$ K (the average value of Popescu et al. 2002), for the cold component. They are calibrated to match the 60 and 100 μm fluxes respectively.

The far-IR to mm domain, from 170 μm to ~ 1 cm, is totally unexplored. Submillimetric observation should provide constraints on the cold dust temperature and on the total dust mass of the sample galaxies. From ~ 1 mm to 1 cm, data are needed to estimate the relative contribution of the thermal and synchrotron radio emission.

The dashed line in the centimetric domain, given for all galaxies with more than two detections, represents the power-law regression to the radio continuum data. The best-fit parameters are given in Table 8.

5. Analysis

Previous analyses, each devoted to a limited spectral domain, have attempted to interpret the SEDs of galaxies: Gavazzi et al. (2002a) for the continuum stellar radiation, Boselli et al. (1998, 2003 and in preparation) for the mid-IR emission, Popescu et al. (2002) for the FIR emission, and Niklas et al. (1997) for the radio emission. In this work, for the first time we analyze the SEDs as determined in the whole spectral range.

5.1. The template SED

The template SEDs in bins of morphological type and luminosity are obtained as median combinations of the normalized (to the K band) SEDs. We used only the detected values and imposed that at least 2 photometric points were available. The resulting extinction corrected template SEDs in different classes of morphological type and luminosity are shown in Figs. 3a and c respectively. The observed (dust attenuated) SEDs of

M 82 and Arp220 (from Elbaz et al. 2002), are given for comparison in Figs. 3b and 3d. The median values of $F(\lambda)/F(K)$ for the templates in the 18 bands considered in this work are given in Table 9, while the fitting models in the visible (corrected and uncorrected for dust extinction) and in the FIR are given in Tables 10, 11 and 12 respectively⁴. The values in parenthesis in Table 9 give the total number of objects in each Hubble type and wavelength bin that were combined to form the templates.

By analyzing Fig. 3 we can observe that: a) the relative contribution to the SED of the young stellar component, emitting in the UV, and of the relatively cold dust emitting at ~ 60 – 200 μm increases from early to late-type spirals and/or from high-mass to low-mass objects; b) the 60 to 100 μm flux density ratio increases with the total FIR emission, indicating a general increase of the big grains dust temperature from massive Sa to low-luminosity Scd-Im-BCD and, to a much higher degree, in starburst galaxies. c) optically selected spirals have UV to near-IR SEDs similar to those of starburst galaxies such as M 82 or Arp 220, despite the fact that these extreme objects have dust attenuations several order of magnitudes higher than normal galaxies, $A(\text{UV}) \sim 1$ for optically selected spirals vs. $A(\text{UV}) \sim 3.5$ for M 82 (Buat et al. 2002) and $A(\text{UV}) \geq 100$ for Arp 220 (Haas et al. 2001). At the same time the far-IR emission of optically-selected, normal galaxies is more than a factor of 10–100 less important than in starburst galaxies.

It is thus extremely dangerous to use the SEDs of starburst galaxies such as M 82 and Arp 220 as templates of normal late-type galaxies at high redshift, as often done, since these objects may not be representative of the mean late-type galaxy population even at earlier epochs, when star formation was expected to be more active.

5.2. The stellar contribution to the mid-IR emission

The Bruzual & Charlot models fitted to the data trace the stellar emission from 1000 \AA to 10 μm , and can thus be used to estimate the stellar contribution to the emission of our target galaxies at 6.75 μm . The ratio of the total flux (dust plus star) to the stellar flux at 6.75 μm , $[F_{6.75}(d+s)/F_{6.75}(s)]$, determined for all galaxies detected at 6.75 μm , and with available visible or near-IR photometry, is given in Table 8, while the median value for each morphological class in Table 13.

Figure 4 shows the relationship between $[F_{6.75}(d+s)/F_{6.75}(s)]$ and the morphological type. The stellar contribution to the total mid-IR emission of galaxies strongly depends on the morphological type. In early-types ($\leq \text{S0a}$), the emission at 6.75 μm is completely dominated by the photosphere of the cold stellar population (see Table 13). The average stellar contribution to the 6.75 μm emission of spiral galaxies is always important, ranging from $\sim 80\%$ in Sa to $\sim 20\%$ to Sc and Im. In BCD the stellar emission contributes on average at $\sim 50\%$. Given the low detection rate in irregular galaxies (Im and BCD), their average $[F_{6.75}(d+s)/F_{6.75}(s)]$ ratios might be

⁴ A sample of Table 10 is given at the end of the paper; the whole Tables 10–12 are available only in electronic form at the CDS via anonymous ftp to cdsarc.u-strasbg.fr (130.79.128.5) or via <http://cdsweb.u-strasbg.fr/cgi-bin/qcat?J/A+A/402/37>

Table 9. Template dust extinction corrected SEDs.

λ (μm)	Log($F(\nu)/F(K)$)												
	SOa	Sa	Sab-Sb	Sbc-Sc	Scd-Sd	Im	BCD	$L_H < 8.3$	$8.3 \leq L_H < 9$	$9 \leq L_H < 9.8$	$9.8 \leq L_H < 10.5$	$L_H \geq 10.5$	
0.20	-3.22(2)	-2.46(5)	-1.51(5)	-1.04(15)	-0.72(4)	-0.38(7)	-0.36(4)	- (1)	-0.37(11)	-0.87(9)	-1.22(12)	-1.62(10)	
0.37	-1.25(5)	-0.96(10)	-0.92(7)	-0.59(16)	-0.47(6)	-0.26(15)	-0.32(9)	-0.12(3)	-0.28(21)	-0.58(17)	-0.88(15)	-1.06(16)	
0.44	-0.78(6)	-0.42(11)	-0.45(7)	-0.26(22)	-0.16(6)	0.06(21)	-0.10(11)	0.11(4)	-0.03(27)	-0.21(21)	-0.40(19)	-0.53(18)	
0.55	-0.48(6)	-0.21(11)	-0.25(7)	-0.13(22)	-0.07(6)	0.13(21)	-0.04(10)	0.23(3)	0.08(27)	-0.09(21)	-0.18(19)	-0.28(18)	
1.25	0.06(5)	0.07(9)	0.05(6)	-0.02(7)	-(-)	0.19(6)	0.08(2)	0.22(2)	0.19(4)	0.09(3)	0.05(12)	0.06(16)	
1.65	0.13(6)	0.13(10)	0.11(6)	0.13(14)	- (1)	0.15(7)	0.11(2)	0.21(2)	0.15(5)	0.14(7)	0.13(19)	0.12(16)	
2.10	0.00(6)	0.00(11)	0.00(7)	0.00(22)	0.00(6)	0.00(35)	0.00(17)	0.00(20)	0.00(32)	0.00(22)	0.00(19)	0.00(18)	
6.75	-0.95(5)	-0.96(9)	-0.46(7)	-0.14(21)	-0.37(5)	-0.19(14)	-0.57(11)	-0.15(4)	-0.35(18)	-0.34(18)	-0.16(18)	-0.61(17)	
12	- (1)	-0.54(4)	-0.24(7)	0.26(13)	- (1)	- (1)	- (-)	- (-)	- (-)	- (1)	0.13(13)	-0.33(14)	
15	-1.37(5)	-1.30(10)	-0.47(7)	-0.13(21)	-0.14(4)	0.06(9)	-0.48(7)	0.02(2)	-0.30(10)	-0.46(18)	-0.22(19)	-0.63(17)	
25	- (1)	- (1)	-0.40(7)	0.46(13)	- (1)	- (1)	- (1)	- (-)	- (1)	0.72(3)	0.28(11)	-0.10(12)	
60	-0.19(2)	0.19(7)	0.43(7)	1.14(17)	1.29(5)	1.44(6)	1.39(6)	- (-)	1.48(10)	1.18(14)	1.05(14)	0.43(15)	
100	0.36(2)	1.01(6)	0.97(7)	1.63(17)	1.72(5)	1.78(7)	1.65(8)	2.00(3)	1.70(9)	1.67(14)	1.61(13)	0.97(15)	
170	0.36(4)	1.15(5)	1.27(7)	1.78(11)	1.88(4)	1.89(10)	1.93(9)	2.05(4)	1.82(12)	1.83(15)	1.68(10)	1.15(11)	
28000	- (1)	- (1)	-1.55(5)	-1.46(8)	- (-)	- (1)	- (-)	- (-)	- (-)	- (-)	-1.63(9)	-1.44(9)	
63000	-2.46(2)	-2.09(2)	-1.57(5)	-1.08(11)	- (-)	- (1)	- (-)	- (-)	- (-)	- (1)	-1.21(9)	-1.40(12)	
126000	-2.00(3)	-1.68(6)	-1.34(5)	-1.01(10)	- (1)	- (1)	- (1)	- (-)	- (-)	- (1)	-1.10(13)	-1.47(14)	
210000	- (1)	- (1)	-1.31(5)	-0.81(10)	-0.72(2)	0.33(4)	- (1)	- (-)	0.51(3)	-0.72(3)	-0.95(11)	-1.06(10)	

Note: the values in parenthesis give the total number of objects in each Hubble type and wavelength bin that were combined to form the templates.

biased towards objects whose stellar contribution to the mid-IR emission is important, the only ones with detectable $6.75 \mu\text{m}$ flux. The decrease of the dust emission observed in BCD and Im galaxies, however, could be due either to their low metallicity, or to the destruction of the carriers of the *UIB* expected in high UV radiation fields (Boselli et al. 1998). We do not see any strong relationship between the $[F_{6.75}(d+s)/F_{6.75}(s)]$ ratio and the total *K* band luminosity or concentration index parameter. However all galaxies with $C_{31}(K) > 4$ have their mid-IR emission at $6.75 \mu\text{m}$ dominated by stars. Among the ISOCAM resolved galaxies, these objects have also a $C_{31}(6.75 \mu\text{m})$ index >4 (Boselli et al. 2003), suggesting that the spatial distribution of the stellar component dominating the mid-IR emission is similar to that emitting in the near-IR.

In the assumption that the stars dominating the emission at $\sim 7 \mu\text{m}$ have a spatial distribution similar to those emitting in the near-IR, we can re-scale our *K* band images (Boselli et al. 1997) using Table 8 and subtract them from the ISOCAM LW2 images of Boselli et al. (2003) to obtain images of the pure dust emission at $6.75 \mu\text{m}$. We apply this correction, as an exercise to the Sab galaxy VCC 1727 (Fig. 5). The ISOCAM LW2 image at $6.75 \mu\text{m}$ shows a very pronounced nucleus, a clumpy, ring-like structure and a smoothed, diffuse external region. The emitting dust, on the contrary, is mostly located along the ring-like structure. Most of the nuclear and part of the diffuse emission in the $6.75 \mu\text{m}$ image is stellar.

The determination of the stellar contribution to the 12 and $15 \mu\text{m}$ emission of galaxies cannot be easily quantified since the Bruzual & Charlot models are limited to the spectral domain $\lambda \leq 10 \mu\text{m}$. The extrapolation of our fit (Fig. 2) indicates that the stellar contribution can be important at $15 \mu\text{m}$, even though less than at $6.75 \mu\text{m}$.

This result has to be taken in serious consideration when mid-IR deep surveys are used to estimate the star formation

Table 13. The average stellar contribution to the $6.75 \mu\text{m}$ emission for different morphological classes.

Type	$\log[F_{6.75}(d+s)/F_{6.75}(s)]$
SOa	-0.17 ± 0.13
Sa-Sab	0.08 ± 0.33
Sb-Sbc	0.39 ± 0.18
Sc	0.76 ± 0.29
Scd-Sd	0.50 ± 0.30
Sm-Im	0.60 ± 0.37
BCD	0.27 ± 0.31

activity of galaxies at high z , where rest-frame mid-IR fluxes might be dominated by the stellar emission.

5.3. The dust emission

As extensively discussed in Sect. 3.1, in a given galaxy the energy emitted by the various stellar populations and absorbed by dust must equal the total energy radiated in the mid- and far-IR domain. However $A(\text{UV})$ was estimated in Sect. 3.1 just from *FIR*, which is a combination of the 60 and $100 \mu\text{m}$ fluxes, not from the integral of the dust emission as determined on the SEDs. It remains to be checked whether the global extinction $A(1000 \text{ \AA} < \lambda < 10 \mu\text{m})$, which depends on the adopted geometrical model and on the choice of the galactic extinction law, is consistent with the observed mid- and far-IR emission.

The energy of the stellar light absorbed by dust is equal to the difference between the integrals of the stellar SEDs

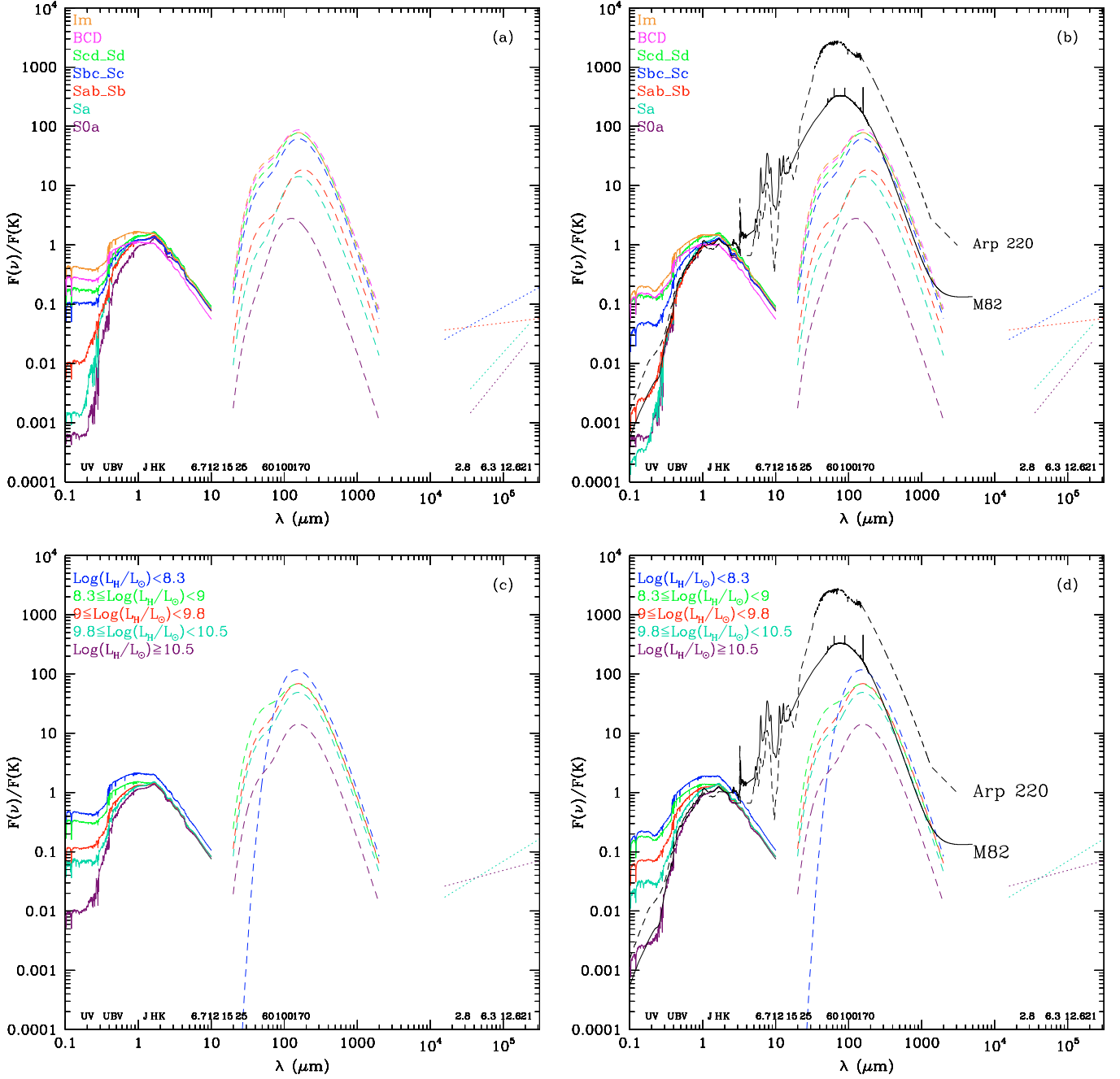


Fig. 3. The extinction corrected **a)** and dust attenuated **b)** template SEDs in bins of morphological type and luminosity (**c), d)**). The dust attenuated SEDs of M 82 (continuum black line) and Arp 220 (dotted black line) are also given for comparison.

(i.e. the Bruzual & Charlot models) prior and after the extinction correction. This should equal the energy radiated in the FIR:

$$\int_{20 \mu\text{m}}^{2000 \mu\text{m}} F(\lambda) d\lambda = \int_{1000 \text{ \AA}}^{10 \mu\text{m}} F_{\text{corr}}(\lambda) d\lambda - \int_{1000 \text{ \AA}}^{10 \mu\text{m}} F_{\text{obs}}(\lambda) d\lambda \quad (8)$$

where the integral on the left is performed under the two modified black-body functions fitted to the data between 20 and 2000 μm (far-IR). The integrals on the right are performed under the Bruzual & Charlot models prior and after the extinction correction. We disregard the dust emission in the range

5–20 μm due to the lack of model fitting in the mid-IR domain, whose energy contribution to the total should however be small.

To illustrate our method we give in Fig. 6 the SED of the galaxy VCC 1554. The energy of the stellar light absorbed by dust is marked by the shaded region shortward of 10 μm , the energy re-emitted in the FIR by the shaded region between 20 and 2000 μm .

Figure 7 shows the relationship between the total energy emitted in the far-IR and that emitted by stars and absorbed by dust in the range between 1000 \AA and 10 μm (Eq. (8)). The median value of the ratio between the energy absorbed by dust and that emitted in the far-IR is 1.27 for the entire sample, 1.03 for

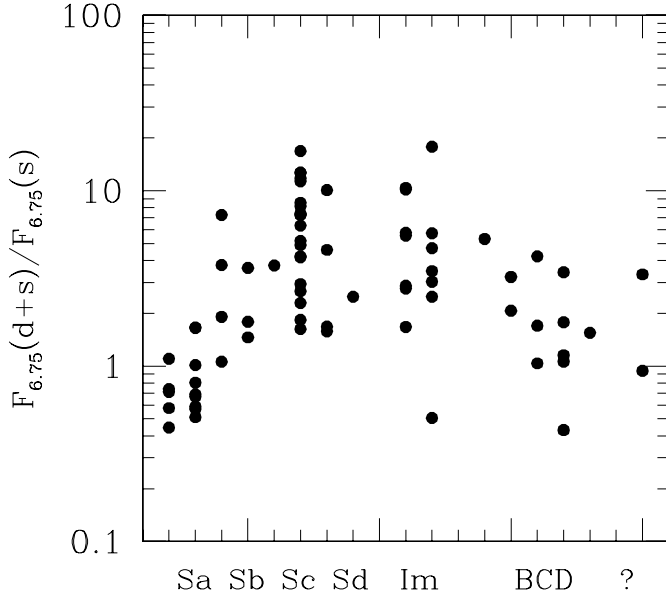


Fig. 4. The relationship between the total flux (dust plus stars) to the stellar flux at $6.75 \mu\text{m}$, $[F_{6.75}(d+s)/F_{6.75}(s)]$, and the morphological type.

those objects whose extinction has been determined directly using the observed FIR/UV ratio, as illustrated in Fig. 8.

The almost linear relation between the absorbed star light and the energy emitted by dust, combined with their ratio close to one, leads us to conclude that the prescription given in Sect. 3.1 to correct stellar SEDs is sufficiently accurate for optically-selected spiral galaxies, even for objects without UV and far-IR data.

The ratio between the energy absorbed by dust and that emitted in the far-IR shows however a weak residual trend with morphological type (Fig. 9) and luminosity (Fig. 10): it is significantly larger than unity in early-type, massive galaxies.

This increase could be due to an underestimate of the far-IR emission of massive, early-type galaxies, that could exist if we missed a colder dust component in quiescent objects with low UV interstellar radiation field.

We remind that the extinction values derived using this prescription are significantly smaller than those obtained using the Calzetti's law, which is probably more accurate for starburst galaxies (see Gavazzi et al. 2002a and Buat et al. 2002 for a detailed discussion on this issue).

5.4. The radio emission

For 25 galaxies detected at more than one frequency in the centimetric domain, we derive the slope of the radio continuum spectrum by a simple linear fit to the data. Excluding galaxies VCC 857, 1110 and 1450 showing large inconsistencies in the radio continuum flux densities and 8 additional objects with signs of nuclear activity (LINER, Seyfert, see Table 2) we obtain an average spectral slope $\alpha = 0.76 \pm 0.27$, consistent with the canonical synchrotron slope $\alpha = 0.8$ found by Niklas et al. (1997) by carefully separating the contribution of the thermal from the synchrotron emission (see Table 8).

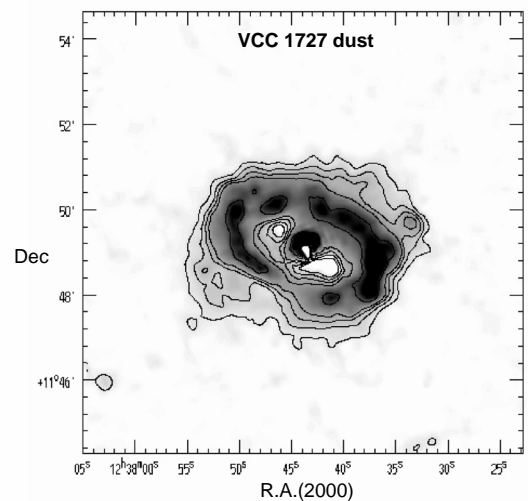
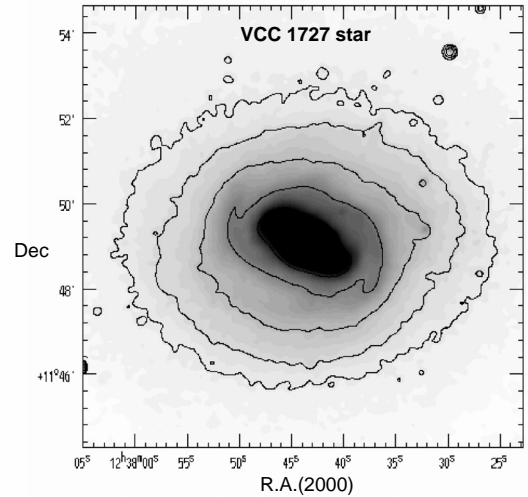
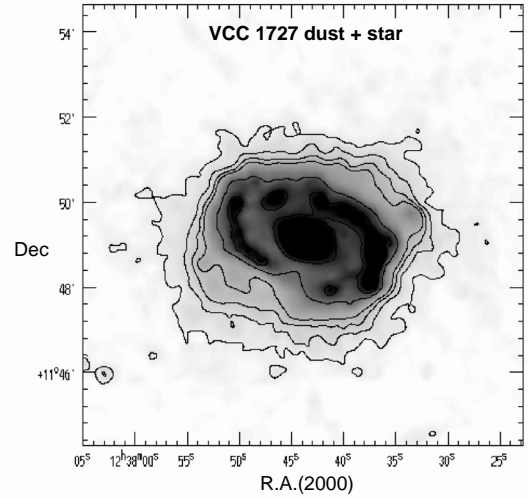


Fig. 5. The gray-level images of the Sab galaxy VCC 1727 at $6.75 \mu\text{m}$: a) the observed images (dust+star), b) the stellar image (scaled from the K band image), c) the image of the dust emission, corrected for stellar contribution (dust). The three images are displayed with the same cuts and on the same scale (6.45×6.45 arcmin).

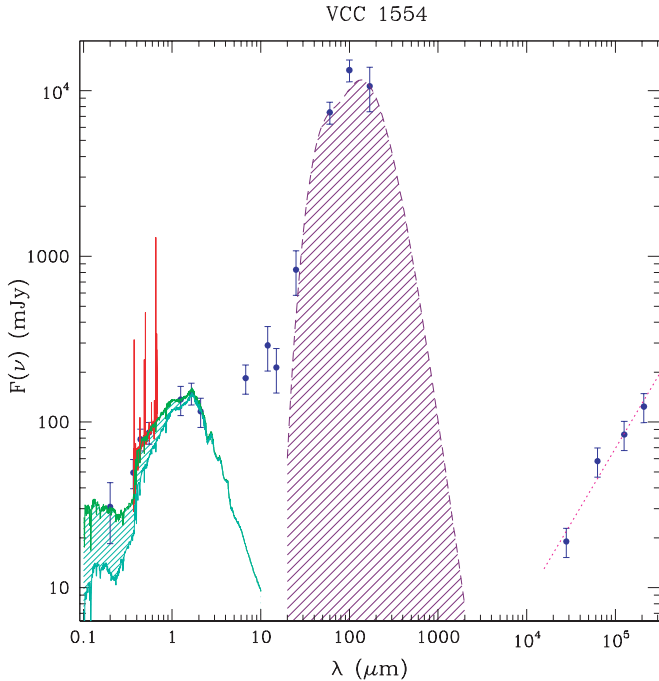


Fig. 6. The SED of the galaxy VCC 1554. The energy of the stellar light absorbed by dust is indicated by the shaded region in between the Bruzual & Charlot extinction corrected model (light green continuum line) and the observed one (emerald green continuum line) in the wavelength range 0.1–10 μm . The energy re-emitted by dust in the FIR is shown by the violet shaded region in the wavelength range 20–2000 μm . The photometric data are shown by blue dots, the optical spectrum is given in red.

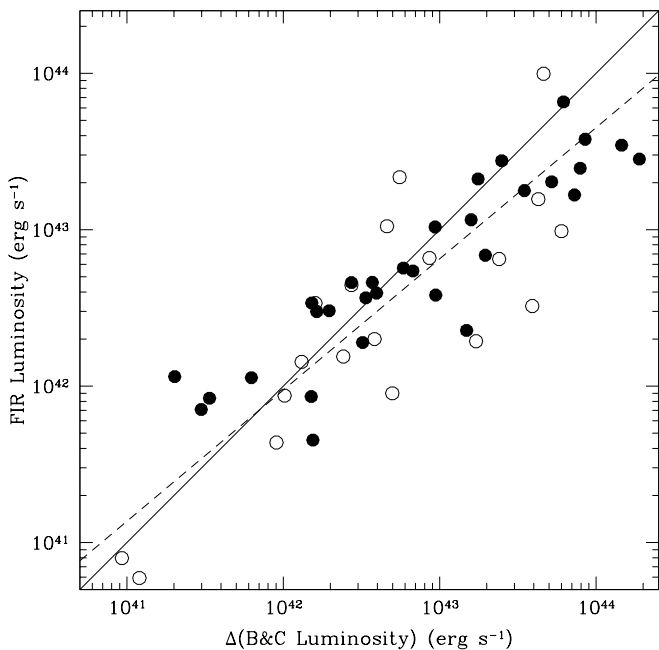


Fig. 7. The relationship between the total energy emitted in the far-IR and that emitted by stars and absorbed by dust in the range between 1000 \AA and 10 μm (see Eq. (8)). The continuum line is the one to one relation, while the dashed line is the bysector fit. Filled symbols are galaxies whose extinction has been determined directly using the observed FIR/UV ratio, empty symbols are objects without far-IR and/or UV data, whose extinction has been determined using the average $A(\text{UV})$ for their morphological type class.

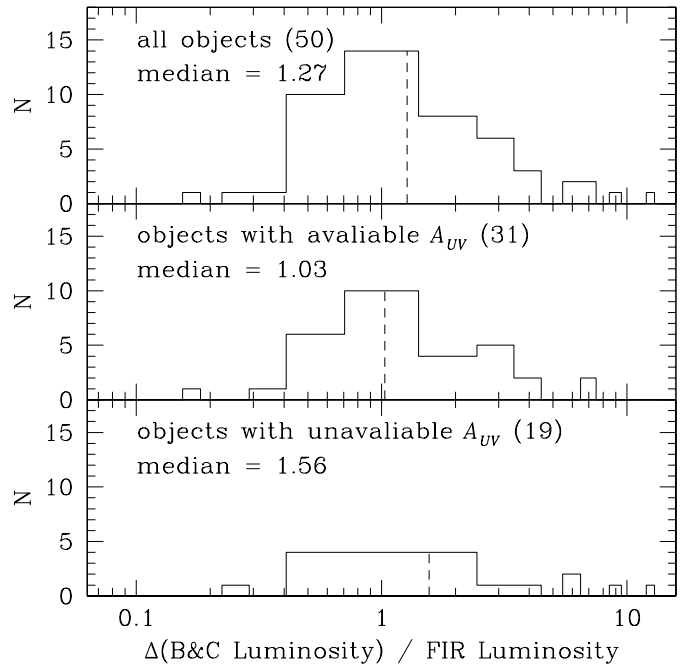


Fig. 8. The distribution of the ratio between the energy absorbed by dust and that emitted in the far-IR for the entire sample **a)**, for galaxies whose extinction has been determined using the observed FIR/UV ratio **b)**, and for those objects without far-IR and/or UV data whose extinction has been determined using the average value of $A(\text{UV})$ for their morphological class **c)**.

5.5. The bolometric luminosity of optically-selected, late-type galaxies

By integrating the fit models in the stellar and FIR domain, we calculate the (observed) bolometric luminosity of our target galaxies:

$$L_{\text{Bol}} = \int_{1000 \text{ \AA}}^{10 \mu\text{m}} F_{\text{obs}}(\lambda) d\lambda + \int_{20 \mu\text{m}}^{2000 \mu\text{m}} F(\lambda) d\lambda. \quad (9)$$

As before, we disregard the contribution of *UIB* and of the very small grains in the 5–50 μm range, thus this estimate gives a lower limits to the total bolometric luminosity.

Figure 11 shows that the bolometric luminosity of optically-selected late-type galaxies in the range $10^8 \leq L_{\text{bol}} \leq 10^{11} L_{\odot}$, is dominated by the stellar emission. The median value of the ratio between the energy emitted by stars in the 1000 \AA –10 μm range and by dust in the Far-IR is 4.0, significantly higher than $f_B/f_{\text{FIR}} \sim 1.6$ found by Soifer et al. (1987) who determined the stellar emission from the *B* band luminosity alone. No relation is observed between the stellar to FIR ratio and the bolometric luminosity, except for an higher dispersion at high luminosity.

Figure 12 shows that the far-IR to bolometric luminosity ratio increases from early Sa spirals ($L_{\text{FIR}}/L_{\text{bol}} \leq 0.1$) to Sc-Sd galaxies ($L_{\text{FIR}}/L_{\text{bol}} \sim 0.2$ –0.4), consistently with Popescu & Tuffs (2002). BCDs have $L_{\text{FIR}}/L_{\text{bol}} \sim 0.2$. The apparent discrepancy with Popescu & Tuffs (2002) who occasionally observed $L_{\text{FIR}}/L_{\text{bol}} > 0.5$ in BCDs is probably due to a systematic

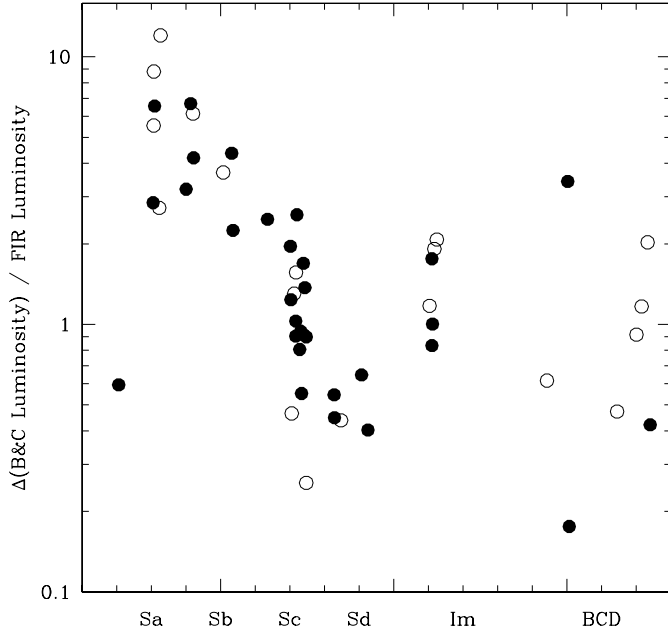


Fig. 9. The ratio between the energy absorbed by dust and that emitted in the far-IR as a function of the morphological type. Symbols as in Fig. 7.

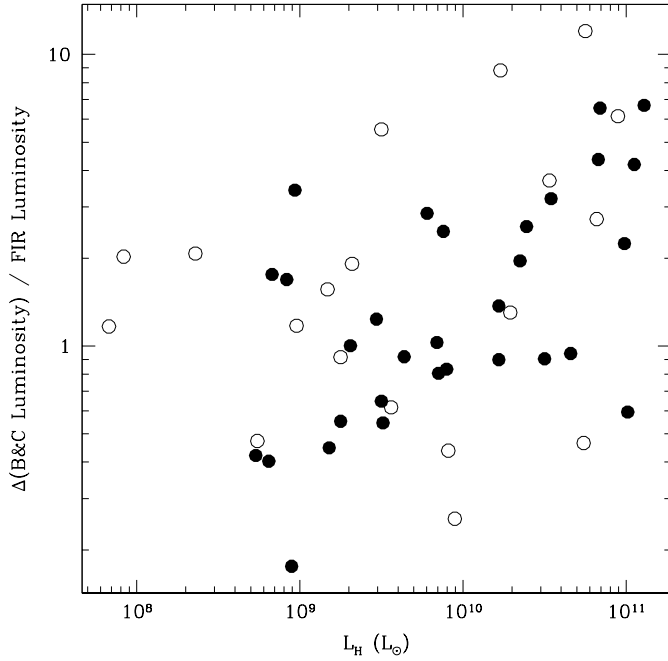


Fig. 10. The ratio between the energy absorbed by dust and that emitted in the far-IR as a function of the H band luminosity. Symbols as in Fig. 7.

difference in determining the stellar contribution to the bolometric luminosity in the two works. We trust our values being based on a robust estimate of the stellar contribution to the bolometric luminosity consequent to a complete and homogeneous spectro-photometric dataset extending from the UV to the near-IR that we have fitted with Bruzual & Charlot population synthesis models.

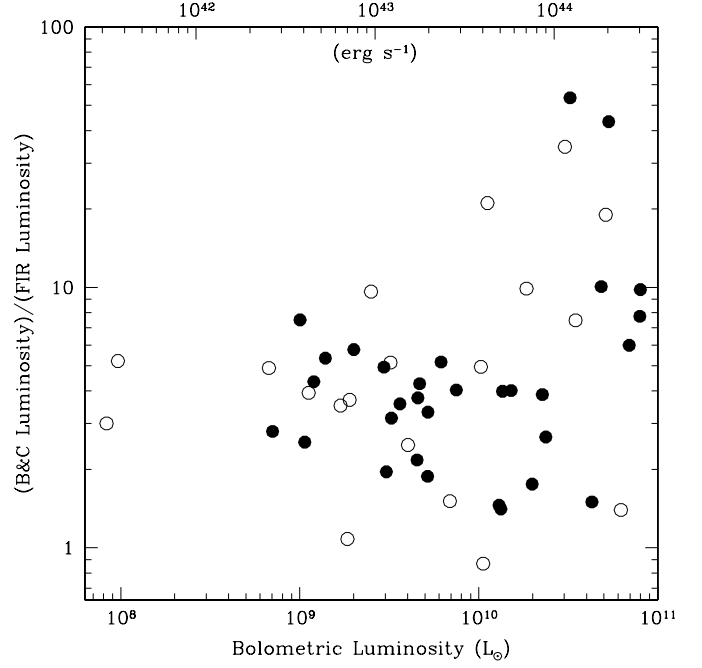


Fig. 11. The relationship of the ratio of the total uncorrected stellar luminosity (from the Bruzual & Charlot model) to the total FIR luminosity versus the bolometric luminosity of the target galaxies. Symbols are as in Fig. 7.

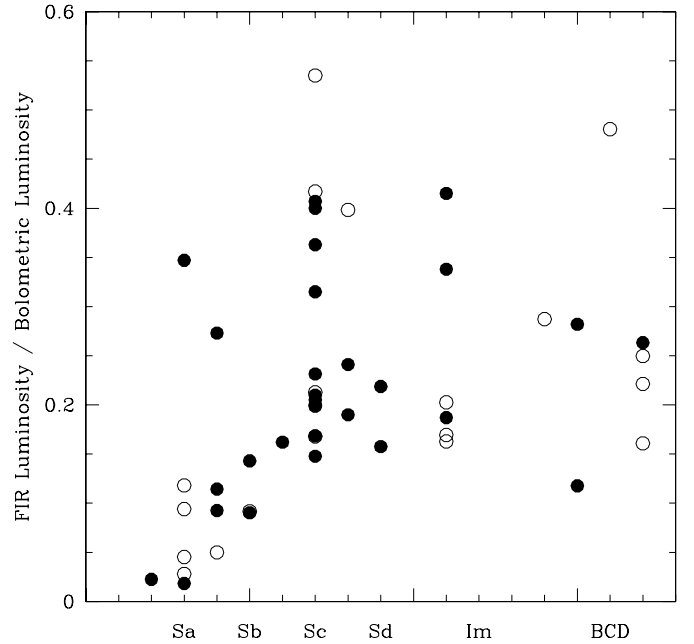


Fig. 12. The relationship between the far-IR to bolometric luminosity ratio and the morphological type. Symbols are as in Fig. 7.

6. Summary and conclusions

We present a multifrequency dataset comprising an optically-selected, volume-limited, complete sample of 118 galaxies in the Virgo cluster. The sample includes all late-type ($\geq S0a$) Virgo A members in the core of the cluster, with projected distance $\Theta < 2$ degrees from M87, or at the periphery of the

cluster ($\Theta > 4$ degrees from the position of maximum projected galaxy density).

The database includes UV, visible, near-IR, mid-IR, far-IR, radio continuum photometric data as well as spectroscopic data on the $H\alpha$, CO and HI lines.

Spectral energy distributions (SEDs) of the individual galaxies, as well as templates SEDs in bins of morphological type and luminosity are derived. The SEDs are fitted with stellar population synthesis models providing an estimate of the total stellar radiation, with modified black-bodies fitted to the far-IR data giving the energy re-emitted by dust, and with power laws representing the synchrotron emission.

Assuming the energy balance between the absorbed stellar light and the energy radiated in the IR by dust, we calibrate an empirical attenuation law suitable for correcting photometric and spectroscopic data of normal galaxies.

The analysis of the SED show that low-luminosity, dwarf galaxies have on average bluer stellar continua and higher far-IR luminosities (per unit galaxy mass) than giant, early-type spirals. Normal spirals have relatively similar observed stellar spectra but 10 to 100 times lower IR luminosities than nearby starburst galaxies such as M 82 and Arp 220. The temperature of the cold dust component increases with the far-IR luminosity, from giant spirals to dwarf irregulars and to a higher extent in starburst galaxies. SEDs of starburst galaxies should not be used as templates of normal high redshift galaxies.

We show that the contribution of the stellar emission to the $6.75 \mu\text{m}$ mid-IR flux is generally important, from $\sim 80\%$ in Sa to $\sim 20\%$ in Sc.

Acknowledgements. We thank J. Donas and D. Pierini for providing us with unpublished UV and near-IR data. We thank S. Arnouts, V. Buat and M. Sauvage for stimulating discussions, and D. Elbaz for providing us with the SED of M 82 and Arp 220. This research has made use of the NASA/IPAC Extragalactic Database (NED) which is operated by the Jet Propulsion Laboratory, California Institute of Technology, under contract with the National Aeronautics and Space Administration. most of the data presented in this work are available through the WEB page <http://goldmine.mib.infn.it>

Appendix: *UBV* CCD photometry of Virgo galaxies⁵

The present work is partly based on new CCD optical photometry of 36 galaxies obtained at the 1.20 m Newton telescope at the Observatoire de Haute Provence (OHP, France), at the 0.9 m telescope at Kitt Peak and at the 2.5 m INT telescope at La Palma. The OHP and the INT observations were taken during the $H\alpha$ surveys presented in Boselli & Gavazzi (2002) and Boselli et al. (2002a) respectively. Details on the observations and data reduction procedures are found in these papers. Kitt Peak targets were observed as fillers during an $H\alpha$ survey of isolated galaxies.

⁵ The Observatoire de Haute Provence (OHP) (France), is operated by the French CNRS; the INT telescope is operated on the island of La Palma by the ING team in the Spanish Observatorio del Roque de Los Muchachos of the Instituto de Astrofísica de Canarias; KPNO is operated by AURA, Inc. under contract to the National Science Foundation.

The $f/6$ 1.2 m OHP telescope was equipped with a thinned TK1024 \times 1024 pixels CCD detector, with a pixel size of 0.69 arcsec and a field of view of 11.8×11.8 arcmin. At the adopted gain, the electron/adu conversion is $3.5 e^-/\text{adu}$, with a readout noise of $8.5 e^-$. Thirty galaxies of the present sample were observed during 26 nights in two runs, in 1998 and 2000. Fourteen galaxies were imaged in the *V*, 30 in the *B* and 1 in the *U* band. The observations were done in poor seeing conditions, ranging from 2 to 4 arcsec. The typical integration time was 10 minutes in the *V*, 15 in the *B* and 30 in the *U* bands.

INT *B* band imaging of 2 galaxies were obtained in 1999 using the Wide Field Camera (WFC) attached at the prime focus of the $f/3.29$ 2.5 m telescope. The WFC is composed by a science array of four thinned AR coated EEV 4K \times 2K CCDs, plus a fifth acting as autoguider. The pixel scale at the detectors is $0.33 \text{ arcsec pixel}^{-1}$, which gives a total field of view of about $34 \times 34 \text{ arcmin}^2$. The observations were done during photometric conditions, with an average seeing of 1.5–2 arcsec and an integration time of 10 min.

Kitt Peak *B* band imaging of 5 galaxies were obtained during 4 nights in 1995 using the 0.9 m telescope in the $f/13$ configuration, equipped with a T2KA 2048 \times 2048 pixel CCD, with a pixel size of $0.384 \text{ arcsec pixel}^{-1}$ and a total field of view of $13.1 \times 13.1 \text{ arcmin}$. At the adopted gain, the electron/adu conversion is $2 e^-/\text{adu}$, with a lecture noise of $4 e^-$. The observations were done during non photometric conditions, with an average seeing of 1–1.5 arcsec and an integration time of 15 min.

The observations were calibrated and transformed into the Johnson *UBV* system using standard stars in the catalogue of Landolt (1983). Observations of the standard stars were repeated every 2 hours. Repeated measurements gave <0.10 mag differences, which we assume as the typical uncertainty of the photometric result given in this work. Not all frames were obtained in photometric conditions. When the zero point was varying by more than 0.05 mag due to cirrus, we choose to observe only galaxies with available multiaperture photometry in order to perform the calibration a posteriori.

The data reduction of the CCD images follows a procedure identical to the one described in previous papers of the series (Gavazzi et al. 1995), based on the IRAF STSDAS data reduction packages. To remove the detector response each image is bias subtracted and divided by the mean of 5 flat field exposures obtained on the twilight sky. Direct inspection of the frames allows manual cosmic rays removal and subtraction of contaminating objects, such as nearby stars and galaxies. The sky background is determined in each frame in concentric object-free annuli around the object. The typical uncertainty on the mean background is estimated 10% of the rms in the individual pixels. This represents the dominant source of error in low S/N regions. The determination of object centroid is performed by fitting Gaussian two-dimensional profiles to the data, centered on the brightest excess in each object, generally corresponding to the nucleus. At the central coordinates determined, a growth curve is derived for each object by integrating the counts in concentric circular rings of increasing radii. The obtained growth curves, transformed from counts to magnitudes, are then compared with the multiaperture

Table 10. Example of template dust extinction corrected B&C SEDs.

λ (μm)	$\text{Log}(F(\nu)/F(K))$												
	S0a	Sa	Sab-Sb	Sbc-Sc	Scd-Sd	Im	BCD	$L_H < 8.3$	$8.3 \leq L_H < 9$	$9 \leq L_H < 9.8$	$9.8 \leq L_H < 10.5$	$L_H \geq 10.5$	
0.1005	-3.26	-2.88	-2.04	-1.03	-0.81	-0.58	-0.40	-0.36	-0.51	-0.97	-1.26	-2.08	
0.1015	-3.25	-2.88	-2.06	-1.05	-0.83	-0.62	-0.44	-0.40	-0.55	-1.01	-1.25	-2.09	
0.1025	-3.36	-3.02	-2.25	-1.28	-1.02	-0.85	-0.67	-0.63	-0.77	-1.24	-1.42	-2.28	
0.1035	-3.28	-2.91	-2.10	-1.09	-0.87	-0.65	-0.46	-0.43	-0.57	-1.04	-1.30	-2.13	
0.1045	-3.19	-2.83	-1.98	-0.98	-0.75	-0.55	-0.37	-0.34	-0.48	-0.95	-1.16	-2.02	
0.1055	-3.20	-2.83	-1.98	-0.97	-0.75	-0.54	-0.36	-0.32	-0.47	-0.93	-1.17	-2.01	
...	
1.0025	-0.02	0.14	0.08	0.08	0.15	0.05	0.22	0.32	0.18	0.12	0.11	0.06	
1.0075	-0.02	0.13	0.07	0.08	0.15	0.04	0.21	0.32	0.17	0.12	0.10	0.05	
1.0125	-0.02	0.14	0.08	0.08	0.15	0.05	0.22	0.33	0.18	0.12	0.11	0.06	
1.0175	-0.02	0.14	0.08	0.08	0.15	0.05	0.22	0.32	0.18	0.12	0.10	0.06	
1.0225	-0.01	0.14	0.08	0.08	0.15	0.05	0.22	0.32	0.18	0.12	0.11	0.06	
...	
9.7800	-1.09	-1.05	-1.10	-1.09	-1.02	-1.24	-1.06	-0.96	-1.10	-1.06	-1.07	-1.10	
9.8200	-1.09	-1.05	-1.10	-1.09	-1.02	-1.24	-1.07	-0.96	-1.11	-1.06	-1.07	-1.11	
9.8600	-1.09	-1.05	-1.11	-1.09	-1.02	-1.24	-1.07	-0.96	-1.11	-1.07	-1.07	-1.11	
9.9000	-1.10	-1.05	-1.11	-1.09	-1.02	-1.24	-1.07	-0.96	-1.11	-1.07	-1.07	-1.11	
9.9400	-1.10	-1.06	-1.11	-1.10	-1.03	-1.25	-1.08	-0.97	-1.12	-1.07	-1.08	-1.11	
9.9800	-1.10	-1.06	-1.12	-1.11	-1.03	-1.25	-1.08	-0.97	-1.12	-1.08	-1.08	-1.12	
10.0200	-1.11	-1.07	-1.12	-1.11	-1.04	-1.26	-1.09	-0.98	-1.12	-1.08	-1.09	-1.12	

Notes: Table 10, 11 (template dust extinction uncorrected) and 12 (template FIR fit) are available only in electronic form at the CDS.

photometry available in the literature, in order to check our photometric calibration and to obtain a zero point for those objects observed in non-photometric conditions. At this stage stars projected within the target galaxies were not subtracted since, unless specified, reference aperture photometry usually includes them. Once the accurate zero point is obtained for each galaxy, a similar procedure is repeated after subtracting contaminating stars and galaxies. Following the procedure described in Gavazzi & Boselli (1996), a magnitude is obtained after integrating along circular, concentric annuli up to the isophotal 25 mag arcsec⁻² B diameter. To improve the photometric accuracy, this procedure is applied adding our measurements with aperture photometry available in the literature. UBV magnitudes of the target galaxies are given in Table 3. The estimated error on the magnitude is $\sim 10\%$.

References

- Almoznino, E., & Brosch, N. 1998, *MNRAS*, 298, 920
- Binggeli, B., Sandage, A., & Tammann, G. 1985, *AJ*, 90, 1681 (VCC)
- Binggeli, B., Popescu, C., & Tammann, G. 1993, *A&AS*, 98, 275
- Boselli, A., & Gavazzi, G. 1994, *A&A*, 283, 12
- Boselli, A., & Gavazzi, G. 2002, *A&A*, 2002, 386, 124
- Boselli, A., Casoli, F., & Lequeux, J. 1995, *A&AS*, 110, 521
- Boselli, A., Tuffs, R., Gavazzi, G., Hippelein, H., & Pierini, D. 1997, *A&A*, 121, 507
- Boselli, A., Lequeux, J., Sauvage, M., et al. 1998, *A&A*, 335, 53
- Boselli, A., Iglesias-Paramo, J., Vilchez, J., & Gavazzi, G. 2002a, *A&A*, 386, 134
- Boselli, A., Lequeux, J., & Gavazzi, G. 2002b, *A&A*, 384, 33
- Boselli, A., Sauvage, M., Lequeux, J., Donati, A., & Gavazzi, G. 2003, *A&A*, in press
- Bothun, G., Mould, J., Caldwell, N., & Mac Gillivray, H. 1986, *AJ*, 92, 1007
- Bottinelli, L., Gougouenheim, L., Fouque, P., & Paturel, G. 1990, *A&AS*, 82, 391
- Bouchet, P., Lequeux, J., Maurice, E., Prevot, L., & Prevot-Burnichon, M. 1985, *A&A*, 149, 330
- Bruzual, G., & Charlot, S. 1993, *ApJ*, 405, 538
- Buat, V., Donas, J., Milliard, B., & Xu, C. 1999, *A&A*, 352, 371
- Buat, V., Boselli, A., Gavazzi, G., & Bonfanti, C. 2002, *A&A*, 383, 801
- Bursetin, D., & Heiles, C. 1982, *AJ*, 87, 1165
- Bursetin, D., Davies, R., Dressler, A., et al. 1987, *ApJS*, 64, 601
- Calzetti, D. 2001, *PASP*, 113, 1449
- Combes, F., Dupraz, C., Casoli, F., & Pagani, L. 1988, *A&A*, 203, L9
- Condon, J. 1987, *ApJS*, 65, 485
- Condon, J., Helou, G., Sanders, D., & Soifer, B. 1990, *ApJS*, 73, 359
- Condon, J., Cotton, W., Greisen, E., et al. 1998, *AJ*, 115, 1693 (NVSS)
- Connolly, A., Szalay, A., Bershad, M., Kinney, A., & Calzetti, D. 1995, *AJ*, 110, 1071
- Deharveng, J. M., Sasseen, T., Buat, V., et al. 1994, *A&A*, 289, 715 (FAUST)
- Deharveng, J. M., Boselli, A., & Donas, J. 2002, *A&A*, 393, 843
- de Vaucouleurs, G., de Vaucouleurs, A., & Buta, R. 1981, *AJ*, 86, 1429
- Donas, J., Deharveng, J. M., Laget, M., Milliard, B., & Huguenin, D. 1987, *A&A*, 180, 12
- Dressel, L., & Condon, J. 1978, *ApJS*, 36, 53
- Elbaz, D., Cesarsky, C. J., Chanial, P., et al. 2002, *A&A*, 384, 848
- Frueh, M. L., Corwin, H. G., de Vaucouleurs, G., & Buta, R. 1996, *AJ*, 111, 722
- Gallagher, J., & Hunter, D. 1986, *AJ*, 92, 557
- Gavazzi, G., & Boselli, A. 1996, *Astro. Lett. and Comm.*, 35, 1
- Gavazzi, G., & Boselli, A. 1999, *A&A*, 343, 86
- Gavazzi, G., Garilli, B., Carrasco, L., Boselli, A., & Cruz-Gonzalez, I. 1994, *A&AS*, 104, 271
- Gavazzi, G., Boselli, A., & Carrasco, L. 1995, *A&AS*, 112, 257
- Gavazzi, G., Boselli, A., Scoddeggio, M., Pierini, D., & Belsole, E. 1999, *MNRAS*, 304, 595
- Gavazzi, G., Franzetti, P., Scoddeggio, M., Boselli, A., & Pierini, D. 2000, *A&A*, 361, 863
- Gavazzi, G., Zibetti, S., Boselli, A., et al. 2001, *A&A*, 372, 29
- Gavazzi, G., Bonfanti, C., Sanvito, G., Boselli, A., & Scoddeggio, M. 2002a, *ApJ*, 576, 135
- Gavazzi, G., Boselli, A., Pedotti, P., Gallazzi, A., & Carrasco, L. 2002b, *A&A*, 386, 114
- Gavazzi, G., Boselli, A., Donati, A., Franzetti, P., & Scoddeggio, M. 2003, *A&A*, 400, 451
- Giovanardi, C., Krumm, N., & Salpeter, E. 1983, *AJ*, 88, 1719
- Haas, M., Klaas, U., Müller, S., Chini, R., & Coulson, I. 2001, *A&A*, 367, L9
- Haynes, M., & Giovanelli, R. 1984, *AJ*, 89, 758

- Haynes, M., & Giovanelli, R. 1986, *ApJ*, 306, 466
- Heller, A., Almozrino, E., & Brosch, N. 1999, *MNRAS*, 304, 8
- Helou, G., Salpeter, E., Giovanardi, C., & Krupp, N. 1981, *ApJS*, 46, 267
- Helou, G., Salpeter, E., & Terzian, Y. 1982, *AJ*, 87, 1443
- Helou, G., Hoffman, G., & Salpeter, E. 1984, *ApJS*, 55, 433
- Helou, G., Khan, I., Malek, L., & Boehmer, L. 1988, *ApJS*, 68, 151
- Hoffman, L., Helou, G., Salpeter, E., Glosson, J., & Sandage, A. 1987, *ApJS*, 63, 247
- Hoffman, L., Williams, H., Salpeter, E., Sandage, A., & Binggeli, B. 1989a, *ApJS*, 71, 701
- Hoffman, G., Lewis, B., Helou, G., Salpeter, E., & Williams, B. 1989b, *ApJS*, 69, 65
- Huchtmeier, W., Richter, O., Bohnenstengel, H., & Hauschildt, M. 1989, *A General Catalogue Of Hi Observations Of External Galaxies* (New York: Springer-Verlag)
- Kenney, J., & Young, J. 1988, *ApJS*, 66, 261
- Kinney, A., Bohlin, R., Calzetti, D., Panagia, N., & Wyse, R. 1993, *ApJS*, 86, 5
- Koopmann, R., Kenney, J., & Young, J. 2001, *ApJS*, 135, 125
- Kotanyi, C. 1980, *A&AS*, 41, 421
- Isobe, T., & Feigelson, E. 1992, *ApJS*, 79, 197
- Lampton, M., Deharveng, J. M., & Bowyer, S. 1990, in *The Extragalactic Background Radiation*, ed. S. Bowyer, & C. Leinert (Dordrecht: Kluwer), IAU Symp., 139, 449
- Landolt, A. 1983, *AJ*, 88, 439
- Longo, G., de Vaucouleurs, A., & Corwin, H. 1983, *A Catalogue of Photoelectric Magnitudes and Colors in the *UBV* System of 3578 Galaxies Brighter than 16th *V* Magnitude (1936–1982)* (University of Texas, Austin)
- Longo, G., & de Vaucouleurs, A. 1985, *A General Catalogue of Photoelectric Magnitudes and Colors of Galaxies in the *UBV* System – Supplement* (University of Texas, Austin)
- Lonsdale, C., Helou, G., Good, J., & Rice, W. 1985, in *Catalogued galaxies and quasars observed in the IRAS survey*, JET Propulsion Laboratory
- Magri, C. 1994, *AJ*, 108, 896
- Mathis, J. 1990, *ARA&A*, 28, 37
- Milliard, B., Donas, J., & Laget, M. 1991, *Ad. Space Res.*, 11, 135
- Niklas, S., Klein, U., & Wielebinski, R. 1995, *A&A*, 293, 56
- Niklas, S., Klein, U., & Wielebinski, R. 1997, *A&A*, 322, 19
- Nilson, P. 1973, *Uppsala General Catalogue of Galaxies* (Uppsala Obser. Annu. vol. 6) (UGC)
- Popescu, C., & Tuffs, R. 2002, *MNRAS*, 335, L41
- Popescu, C., Tuffs, R., Völk, H., Pierini D., & Madore B. 2002, *ApJ*, 567, 221
- Prugniel, P., & Heraudeau, P. 1998, *A&AS*, 128, 299
- Rush, B., Malkan, M., & Spinoglio, L. 1993, *ApJS*, 89, 1
- Sage, L., & Wrobel, J. 1989, *ApJ*, 344, 204
- Sandage, A., Binggeli, B., & Tammann, G. A. 1985, *AJ*, 90, 1759
- Savage, B., & Mathis, J. 1979, *ARA&A*, 17, 73
- Schmitt, H., Kinney, A., Calzetti, D., & Storchi Bergmann, T. 1997, *AJ*, 114, 592
- Schneider, S., Thuan, T., Magri, C., & Wadiak, J. 1990, *ApJS*, 72, 245
- Schroeder, A., & Visvanathan, N. 1996, *A&AS*, 118, 441
- Soifer, B., Sanders, D., Madore, B., et al. 1987, *ApJ*, 320, 238
- Soifer, B., Boehmer, L., Neugebauer, G., & Sanders, D. 1989, *AJ*, 98, 766
- Stark, A., Knapp, G., Bally, J., et al. 1986, *ApJ*, 310, 660
- Takamiya, M., Kron, R. G., & Kron, G. E. 1995, *AJ*, 110, 1083
- Thuan, T., & Sauvage, M. 1992, *A&AS*, 92, 749
- Tuffs, R., Popescu, C., Pierini, D., et al. 2002, *ApJS*, 139, 37
- Warmels, R. 1986, Ph.D. Thesis
- Witt, A. N., & Gordon, K. D. 2000, *ApJ*, 528, 799
- Xilouris, E., Byun, Y., Kylafis, N., Paleologou, E., & Papamastorakis, J. 1999, *A&A*, 344, 868
- Young, J., Allen, L., Kenney, J., Lesser, A., & Rownd, B. 1996, *AJ*, 112, 1903
- Zwicky, F., Herzog, E., Karpowicz, M., Kowal, C., & Wild, P. 1961–1968, *Catalogue of Galaxies and of Cluster of Galaxies* (Pasadena, California Institute of Technology; CGCG)